ADVANCED MATERIALS
www.advmat.de

Defect-Free Nanowelding of Bilayer SnSe Nanoplates

Jing-Rong Ji, John W. Villanova, Salvador Barraza-Lopez, Stuart S. P. Parkin,* and Kai Chang**

Nanowelding is a bottom-up technique to create custom-designed nanostructures and devices beyond the precision of lithographic methods. Here, a new technique is reported based on anisotropic lubricity at the van der Waals interface between monolayer and bilayer SnSe nanoplates and a graphene substrate to achieve precise control of the crystal orientation and the interface during the welding process. As-grown SnSe monolayer and bilayer nanoplates are commensurate with graphene's armchair direction but lack commensuration along graphene's zigzag direction, resulting in a reduced friction along that direction and a rail-like, 1D movement that permits joining nanoplates with high precision. This way, molecular beam epitaxially grown SnSe nanoplates of lateral sizes 30–100 nm are manipulated by the tip of a scanning tunneling microscope at room temperature. In situ annealing is applied afterward to weld contacting nanoplates without atomic defects at the interface. This technique can be generalized to any van der Waals interfaces with anisotropic lubricity and is highly promising for the construction of complex quantum devices, such as field effect transistors, quantum interference devices, lateral tunneling junctions, and solid-state qubits.

1. Introduction

Miniaturized electronic components such as FinFET devices and next-generation Gate-All-Around (GAA) devices are formed from 3D heterostructures; their construction necessitates the precise joining of different materials with various shapes along the vertical and lateral directions. From the perspective of device design and characterization, novel techniques for creating sub-10 nm scale semiconductor nanostructures with predesigned shapes are urgently needed. However, this is not an easy task because top-down lithographic methods inevitably introduce disorder at the boundaries and interfaces between different materials (also leaving chemical residues in the process), while bottom-up growth methods encounter significant difficulty in controlling the dimensions of nanostructures in all three directions. In contrast, and as a method that combines nanoscale manipulation and local coalescence of nanocrystals, nanowelding provides a promising approach for the controlled creation of nanostructures.[1]

Nanowelding has been demonstrated in carbon nanotubes,[2–6] metallic nanowires,[7–15] metallic nanoparticles,[16] semiconducting nanowires,[17] semiconducting nanoparticles,[18] and ceramic nanowires.[19] It relies on methods such as global heating,[3,7,11,15,18] electron beam exposure,[2,19] near-field effects,[3,4] cold welding,[8] laser annealing,[4,9,12,14,16] electric current Joule heating,[10] and acid vapor triggering.[13] Since grain boundaries can deteriorate the performance of nanodevices, it is critical to avoid them. However, controllable and seamless nanowelding has never been achieved between semiconducting nanocrystals, nor between nanowires or nanoplates, this being a much more difficult task than the welding of metals like silver or gold.[8]

A seamless nanowelding between semiconductor nanocrystals requires aligning and connecting them with atomic precision, but this has rarely been achieved. Here, we report a method to realize defect-free nanowelding between 2D semiconducting nanoplates that relies on the anisotropic lubricity of the interface between graphene and monolayer or bilayer SnSe. The nanoplates are manipulated by the tip of a scanning tunneling microscope (STM) and contact along their ⟨11⟩ edges, and the welding process simply requires in situ heating. To the best of our knowledge, this is the first time that separate 2D nanoplates are controllably joined. This method can be applied to any 2D nanostructures that display anisotropic friction forces with their supporting substrate.

J.-R. Ji, S. S. P. Parkin
Max Planck Institute of Microstructure Physics
Weinberg 2, 06120 Halle, Germany
E-mail: stuart.parkin@mpi-halle.mpg.de
J. W. Villanova, S. Barraza-Lopez
Department of Physics
University of Arkansas
Fayetteville AR, 72701, USA
E-mail: sbarraza@uark.edu
K. Chang
Beijing Academy of Quantum Information Sciences
Beijing 100193, China
E-mail: changkai@baqis.ac.cn

The ORCID identification number(s) for the author(s) of this article can be found under https://doi.org/10.1002/adma.202312199

DOI: 10.1002/adma.202312199

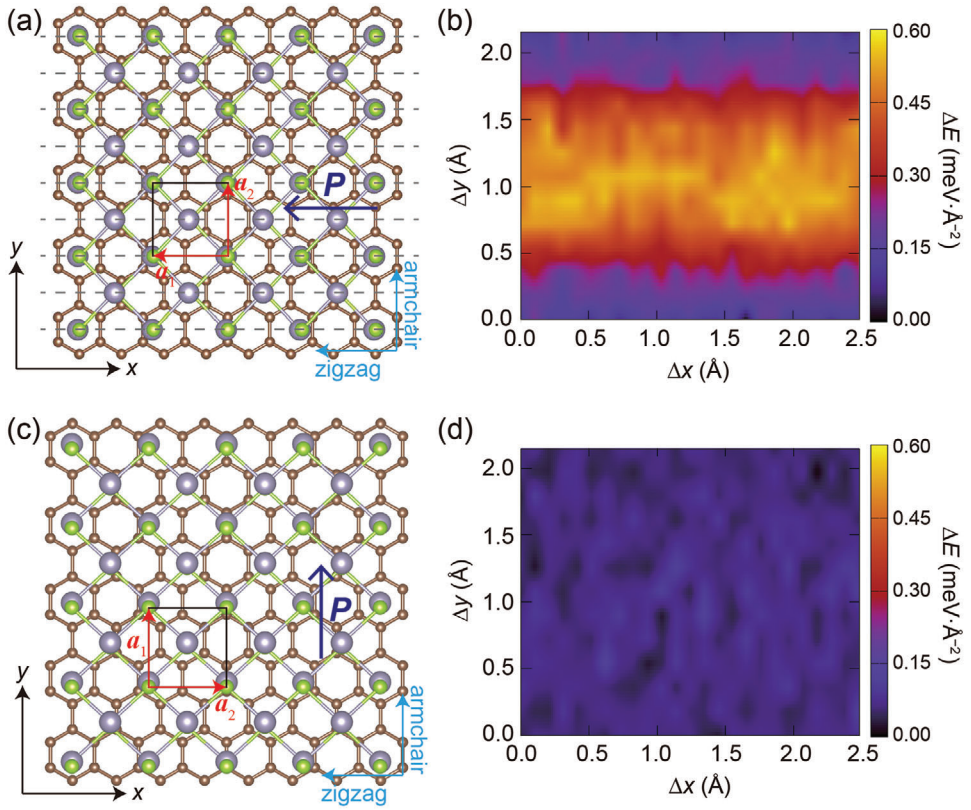

Figure 1. Anisotropic lubricity of monolayer SnSe nanoplates grown on top of a graphene substrate due to uniaxial lattice matching. a) A naturally formed lattice structure of a monolayer of SnSe on graphene. The gray, green, and brown balls are Sn, Se, and C atoms, respectively. The crystalline directions of SnSe and graphene are labeled by red and blue arrows, respectively. The gray dashed lines indicate the valleys between the zigzag chains of graphene, where the Sn and Se atoms sit. b) Energy corrugation landscape of laterally moving SnSe (Δx, Δy) away from the structure in panel (a). c) An incommensurate configuration created by rotating the SnSe 90° from the orientation in panel (a), while keeping the graphene lattice unchanged. d) Energy corrugation landscape corresponding to the structure in panel (c).

2. Results

2.1. Anisotropic Lubricity

Anisotropic lubricity between two atomically clean surfaces has been studied since the 1990s, including the friction force at the interfaces of homojunctions[20–22] and heterojunctions.[23,24] Furthermore, the friction force anisotropy between a sharp tip and a single crystal surface has been extensively characterized by friction force microscopy, a technique developed from atomic force microscopy. Importantly, friction is reduced when the lattices of the contacting surfaces are incommensurate.[25–33] Such an effect lies at the origin of superlubricity at the interfaces between van der Waals materials such as graphite and hexagonal boron nitride (h-BN).[20,22,27,29,34–36] On the other hand, if the lattices are commensurate only along a certain direction at the contact surfaces, the friction force would be enhanced along that direction, thereby restricting sliding to only the orthogonal Cartesian direction, and permitting rotations to very specific angles.[22,23] Such an effect thereby provides a straight, 1D "guiding rail" for the manipulation of nanostructures and it underpins this work.

SnSe monolayers are 2D ferroelectric semiconductors with a 2.1 eV electronic bandgap and an in-plane polarization along the $\boldsymbol{a}_1$ direction.[37] When epitaxially grown on a graphene substrate, their orthorhombic lattice (space group $Pnm2_1$) exhibits the lattice matching conditions shown in **Figure 1a**: the $\boldsymbol{a}_2$ (4.26 Å) direction is highly commensurate with the armchair direction of graphene ($\sqrt{3} \times 2.46$ Å), while the $\boldsymbol{a}_1$ direction (4.35 Å) is incommensurate with graphene's zigzag direction. This uniaxial commensurate condition leads to an anisotropic lubricity (that is, distinctly different barriers for sliding along orthogonal directions) that is revealed from the first principles calculations shown in Figure 1a. The atomistic interface there has been relaxed to an energy minimum, in which the Sn and Se atoms lie between the zigzag chains of graphene.

Figure 1b is a map of ΔE, defined as the energy difference between the energy minimum (starting) configuration seen in Figure 1a and that with a lateral translation (Δx, Δy) of the SnSe monolayer relative to the underlying graphene, without any additional atomistic optimization. The fluctuation of ΔE per unit area along the x (graphene's zigzag)-axis is less than 0.10 meV Å^{-2} (1.6×10^{-3} N m^{-1}), while that along the y-axis is at least six times larger (over 0.60 meV Å^{-2} or 10.0×10^{-3} N m^{-1}), thus precluding the relative motion of monolayer SnSe along the armchair direction of graphene. The maximum of ΔE appears at the positions where $\Delta y = 1.07$ Å, which is exactly $a_2/4$, corresponding to a configuration in which the Sn and Se atoms sit right above

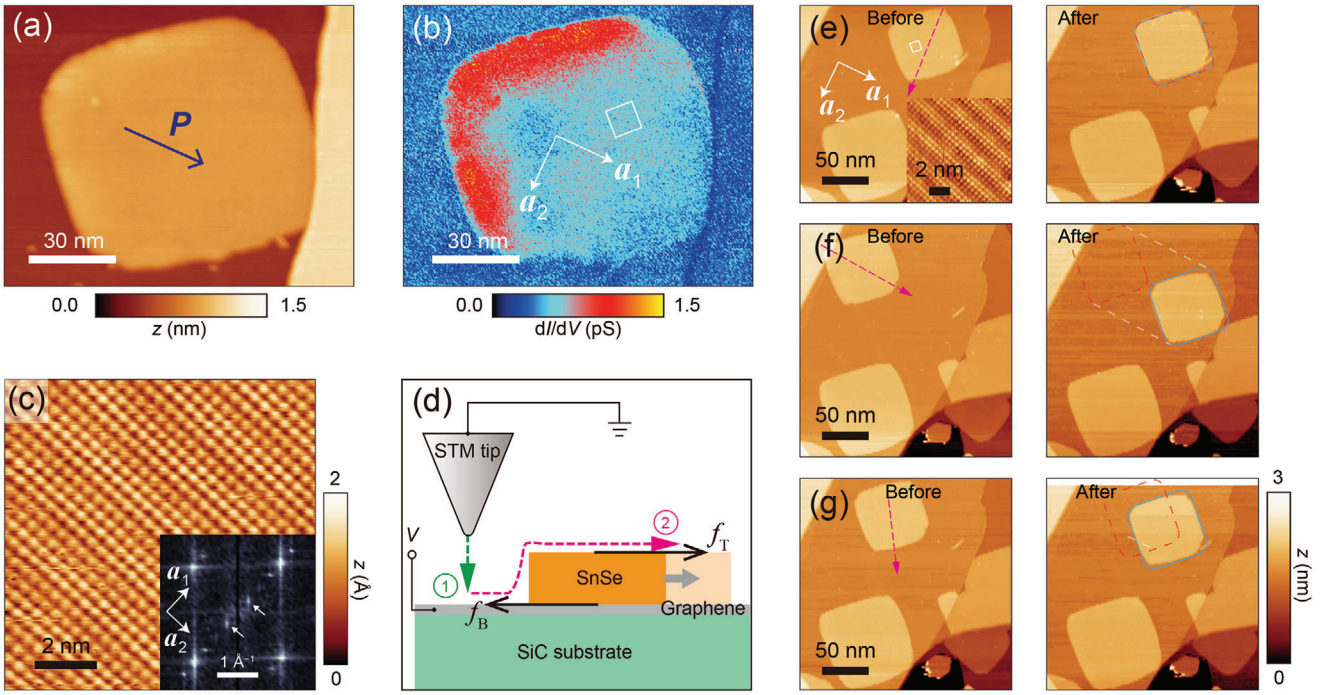

Figure 2. Experimental demonstration of anisotropic lubricity. a) STM topography image and b) simultaneously recorded dI/dV image of a monolayer SnSe nanoplate at room temperature. $V_s = -0.2$ V, $I_t = 2$ pA. c) Atom-resolved image of the monolayer SnSe nanoplate, acquired from the area indicated by the white square in panel (b). $V_s = -20$ mV, $I_t = 500$ pA; inset: Fourier transform. The white arrows label the spots from the moiré pattern between SnSe and graphene. d) Schematic diagram of the process of moving a SnSe nanoplate. e–g) Three pairs of STM topography images showing three typical attempts to move a SnSe nanoplate. $V_s = -0.2$ V, $I_t = 2$ pA. The magenta dashed arrows indicate the paths of the tip. The red dashed and blue solid rectangles are the original and final positions before and after the tip movement. e) Inset: atom-resolved image acquired from the area in the white square. $V_s = -0.2$ V, $I_t = 100$ pA. (Data in panel (a) was acquired from the same area as Figure S6 in the Supplementary Information of Ref. [37]).

the zigzag chains of graphene. This 1D barrier is very different to that observed in the sliding of graphite on graphite and similar homointerfaces with a honeycomb lattice, in which lattice commensuration is recovered once the two homolattices are rotated by multiples of 60°.[27] We also calculated the ΔE landscape for a heterostructure with an incommensurate configuration, which is created by rotating the monolayer SnSe by 90°, aligning its $\boldsymbol{a}_1$ direction parallel with the armchair direction of graphene, and shown in Figure 1c. In this heterostructure, lattice matching vanishes along both in-plane directions, making ΔE lower than 0.1 meV Å^{-2} throughout the (Δx, Δy) space (Figure 1d). This implies that a lack of lattice commensuration along one spatial direction indeed induces a sliding anisotropy at the monolayer SnSe/graphene interface.

The conclusions drawn from the above calculations are consistent with our experimental observations. We prepared SnSe nanoplates with lateral sizes of 30–100 nm, and thicknesses of 1 (monolayer) or 2 (bilayer) layers. All the nanoplates naturally grow along the graphene lattice, with the polarization direction ($\boldsymbol{a}_1$) of SnSe along the zigzag direction of graphene, and have edges oriented along their ⟨11⟩ directions. For a SnSe monolayer, the crystalline orientation can be identified from the dI/dV images measured at a bias voltage close to its valence band maximum, such as −0.2 V (**Figure** 2b). The moiré pattern between SnSe monolayers and graphene gives the orientation of SnSe, and those moiré stripes extend along its $\boldsymbol{a}_2$ direction (Figure 2c). A detailed analysis of the moiré patterns in SnSe monolayers can be found in ref. [37]. We then moved the SnSe monolayer nanoplates with an STM tip, as discussed in the following sections.

To guarantee the repeatability of the nanoplate movements, we used the standard procedure illustrated in Figure 2d; the STM tip is first stabilized at a certain bias voltage V_s on the graphene substrate near the nanoplate (typically −1 or −2 mV), and the setpoint of the tunneling current I_t is increased from imaging conditions (2 pA) up to a target value of several nA, thus bringing the tip closer to the sample's surface. The tip then moves along a straight path across the nanoplate, during which it climbs onto the nanoplate, interacts with the surface of the nanoplate, and pushes it forward along some direction. This movement involves two opposing friction forces exerted on the SnSe nanoplate: f_T between the tip and the nanoplate, and f_B between the nanoplate and graphene. The nanoplate moves with the tip when $|f_T| > |f_B|$.

Figure 2e–g showcases multiple typical instances of monolayer nanoplate motion when $V_s = -2$ mV and the STM tip is moved with a speed of $v = 5$ nm s^{-1}. Moving the tip along the $\boldsymbol{a}_2$ (armchair) direction of the SnSe monolayer barely moved the nanoplate, even when I_t was increased to 7.5 nA (Figure 2e). However, the nanoplate was easily pushed over 90 nm away from its original location when the tip was moved along the $\boldsymbol{a}_1$ direction, using a lower I_t of 2.5 nA (Figure 2f). To experimentally demonstrate the anisotropy of lubricity unambiguously, we moved the tip along a random direction in Figure 2g. Still, the nanoplate only moved along the $\boldsymbol{a}_1$ direction, while no movement

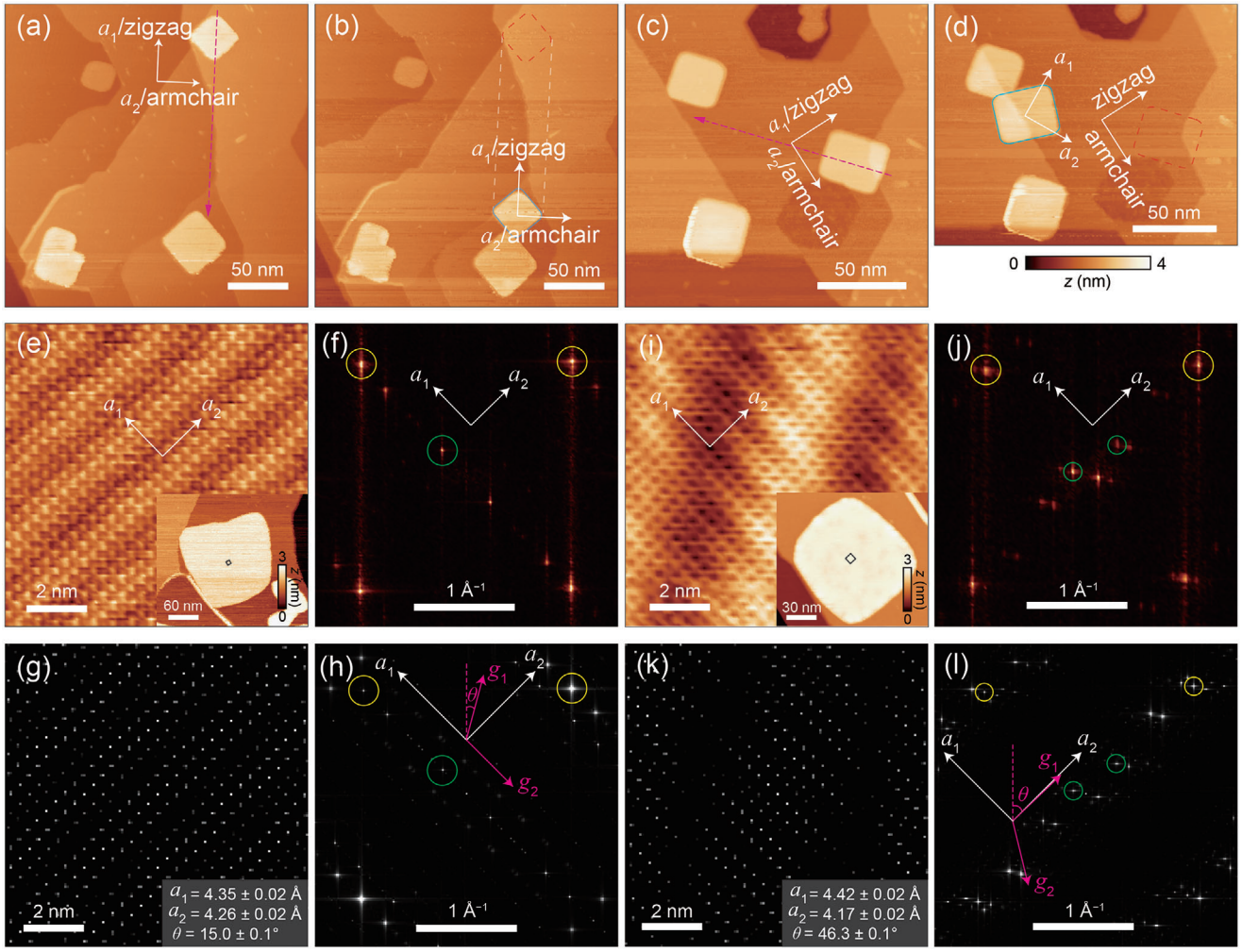

Figure 3. Lubricity and lattice parameters of bilayer SnSe nanoplates. a,b) STM topography images acquired a) before and b) after an attempt to move a bilayer nanoplate along its $\boldsymbol{a}_1$ direction. The nanoplate slides without any rotation. c,d) STM topography images acquired c) before and d) after an attempt to move a bilayer nanoplate along a random direction. The nanoplate is rotated by 28°. The parameters for pushing the nanoplate are $V_s = -1$ mV, $I_t = 2$ nA, $v = 5$ nm s^{-1}. Imaging parameters: $V_s = -0.4$ V, $I_t = 2$ pA. e,f) Atom-resolved topography image of the e) pristine bilayer nanoplate and f) the Fourier transformed (FT) image. $V_s = -50$ mV, $I_t = 250$ pA. e) Inset: topography image of the nanoplate. $V_s = -0.2$ V, $I_t = 2$ pA. The yellow and green circles in panel (f) indicate the Bragg spots of SnSe and the moiré pattern, respectively. g,h) Moiré pattern and the FT image simulated by a MATLAB code superposing the lattices of SnSe and graphene. θ is defined as the angle between the vertical direction and the lattice vector $\boldsymbol{g}_1$ of the underlying graphene lattice, as illustrated in panel (h). i–l) Similar experimental data, and simulated images as those in panels (e)–(h), acquired from a bilayer nanoplate rotated away from the commensurate configuration. Imaging parameters: i) $V_s = -60$ mV, $I_t = 500$ pA, and inset: $V_s = -0.3$ V, $I_t = 2$ pA. e,i) Chopped from larger images for clarity, while the f,j) FT images are generated from Figure S3 (see Figure S4 as well, Supporting Information).

was seen along the $\boldsymbol{a}_2$ direction. These experiments inspired us to manipulate low-dimensional semiconductor nanostructures along a precise direction naturally restricted by the crystalline lattice of the substrate. To test the strength of this restriction, we further increased the f_T along the $\boldsymbol{a}_2$ direction by bringing the tip closer: the nanoplate does not move along $\boldsymbol{a}_2$ and it rather breaks at $V_s = -1$ mV and $I_t = 15$ nA (Figure S1, Supporting Information).

The operation parameters that activate the movement of SnSe nanoplates have a strong dependency on the nanoplate size. Figure S2 (Supporting Information) demonstrates the manipulation of monolayer nanoplates with sizes ranging from 80 nm × 83 nm to 35 nm × 40 nm. In general, moving larger plates requires a closer tip–sample distance (with a concomitant lower bias voltage and a larger tunneling current setpoint), while smaller plates can be moved under less strict conditions. Indeed, when the nanoplate is as small as 35 nm × 40 nm, they can be moved even under imaging conditions, such as −0.4 V and 2 pA.

The motion of SnSe bilayer nanoplates also follows the above anisotropic lubricity principles, but the substrate restriction is less strict. The nanoplate still moves precisely along the $\boldsymbol{a}_1$ direction if the path of the tip does not severely deviate from this direction (**Figure 3a,b**). However, if the motion of the tip is significantly away from the $\boldsymbol{a}_1$ direction, the bilayer nanoplate may now rotate as well. Figure 3c,d shows an example of rotating an ≈30 nm sized bilayer nanoplate by moving the tip 45° away from the $\boldsymbol{a}_1$ direction, applying the tunneling conditions of $V_s = -1$ mV and $I_t = 2$ nA. Once the nanoplate has been rotated, the

anisotropic lubricity is thus no longer in place because the lattice matching to the graphene substrate becomes lifted (see our calculations), and the nanoplate can be further moved along the two in-plane directions.

Interestingly, the alignment between graphene and a bilayer nanoplate also significantly influences the latter's lattice parameters. Most of the as-grown bilayer nanoplates still follow a commensurate lattice restriction, with lattice parameters of $a_1 = 4.35 \pm 0.02$ Å and $a_2 = 4.26 \pm 0.02$ Å, the same as those of monolayer nanoplates.[37] Figure 3e–h illustrates the moiré pattern in a commensurate bilayer nanoplate and the corresponding simulation. However, once a bilayer nanoplate is rotated to an incommensurate alignment, the lattice restriction no longer exists and the lattice parameters evolve according to our moiré pattern simulation, into $a_1 = 4.42 \pm 0.02$ Å and $a_2 = 4.17 \pm 0.02$ Å, close to those of bulk SnSe.[38–40] Unlike few-layer graphene or few-layer transition metal dichalcogenides, the magnitudes of the lattice constants evolve with the number of layers in orthorhombic monochalcogenides,[40] implying that the originally observed commensuration on bilayer SnSe lowers the interface's energy but it creates strain on SnSe. The moiré pattern simulation can help determine the in-plane lattice parameters beyond the STM's intrinsic resolution (typically 0.1 Å) at any temperature, and it is robust against modest drift during the scan (see Section S4 in the Supporting Information). If we assume that the incommensurate bilayer nanoplates are nearly free-standing, then the commensurate bilayer nanoplates experience a compressive strain of −1.58% along the $\boldsymbol{a}_1$ direction and a tensile strain of 2.16% along the $\boldsymbol{a}_2$ direction. Considering that graphene is usually regarded as a substrate with an extremely low surface energy, such values are quite significant but still consistent with expectations.[40] On the other hand, the area of a unit cell is nearly the same for the commensurate (18.53 Å^2) and incommensurate (18.43 Å^2) cases.

2.2. Defect-Free Nanowelding

Now that the technique of nanoplate manipulation has been established, we further demonstrate that nanoplates can be seamlessly merged together. We start from two separate ≈30 nm sized bilayer nanoplates that are 60 nm away from each other (**Figure 4a**). One of the nanoplates is moved toward the other one under the tunneling conditions of $V_s = -1$ mV, $I_t = 1$ nA until they make physical contact (Figure 4b). The grain boundary between the two nanoplates can be clearly seen from the room temperature topography image (Figure 4c).

The edges of the SnSe nanoplates prefer the ⟨11⟩ crystalline directions, along which Sn and Se atoms are alternatively arranged. In principle, twin boundaries or dislocations formed by joining two such edges can be eliminated by annealing at a proper temperature. However, the fluctuation of the SnSe lattice is not large enough at room temperature to form a single-crystalline welding, like that between the nanowires of noble metals.[8] A previous study suggests that ≈10 nm sized PbSe quantum dots begin to merge at 403 K, during which there is certain probability that the crystalline orientation of neighboring quantum dots is automatically aligned, and a defect-free interface is formed.[18] Nevertheless, techniques that guarantee defect-free nanowelding between semiconductor nanostructures are still absent. In our experiments, we use an in situ heater attached to the STM sample stage to anneal the sample while scanning the nanoplates' topography to monitor the welding progress (Figure 4d–j). The grain boundary gradually disappears as the temperature is increased, and vanishes at 420 K. Remarkably, the atom-resolved image in Figure 4k reveals no atomistic defects within the welded region. Furthermore, the overall shape of the nanoplates is well maintained up to 450 K, implying that this technique can be used to eliminate the grain boundaries while also permitting the creation of more complex nanostructures from multiple nanoplates. The nanowelding procedure is well repeatable, and Figure S5 (Supporting Information) provides another example of seamless nanowelding.

The underlying physics behind the defect-free nanowelding process can be understood as follows: since the orientation and movement of the nanoplates strictly follow the lattice of graphene, the basis of the SnSe lattice of both nanoplates is perfectly aligned with each other prior to welding. Thus, before welding, atoms are precisely aligned and separated by a distance slightly larger than the lattice constant of SnSe (**Figure 5a**). At elevated temperatures, the fluctuation of the atoms is enhanced, and when the annealing temperature is high enough, it activates the formation of chemical bonds at the ⟨11⟩ edges of the contacting sections. The formation of new chemical bonds also drags the nanoplates slightly closer along their $\boldsymbol{a}_1$ directions, and remaining "slits" between nanoplates can be considered as molecular vacancies that align into rows. The subsequential evolution of these vacancies follows well-established molecular migration mechanisms such as Fick's laws (Figure 5a). The migration of molecular vacancies eliminates the slits at the interface, and these vacancies will be released when they migrate to the free edges of the nanoplates, hence defect-free nanowelding is achieved.

Since atomistic calculations helped understand the origin of the experimentally observed anisotropic motion of SnSe monolayers and bilayers (Figures 1 and 2), we rely on ab initio molecular dynamics calculations of two monolayer SnSe nanoplates on graphene to describe the evolution of 1D interfaces within nanowelding on a structure containing 1296 atoms. The structure contains a graphene substrate and two SnSe nanoplates with ⟨11⟩ edges. The simulation was run in time basis at 400 K, and technical details of these calculations can be found in the Experimental Section. **Figure 5b,c** shows snapshots of the ab initio molecular dynamics structures at 0.0 and 0.3 ps that show the two nanoplates joining smoothly together. Figure 5d showcases the motion of the geometric centers of graphene and the two SnSe nanoplates during the annealing process. As discussed above, in the first picosecond, the SnSe nanoplates move toward each other along the *x*-direction, which is the zigzag direction of graphene, while little motion happens along the *y*-direction. Figure 5d also displays the effective temperature $T(t)$ during the simulation and the total structural energy (defined in the Experimental Section), where t is the evolution time of the structure.

A perfect crystalline orientation like the one displayed in Figure S6a–d (Supporting Information) is critical to defect-free nanowelding. For comparison, a rare case of misaligned SnSe monolayer nanoplates is shown in Figure S6e–g (Supporting Information). The separation between the atoms at the contacting points is not uniform, and the edge lattice exhibits significant disorder.

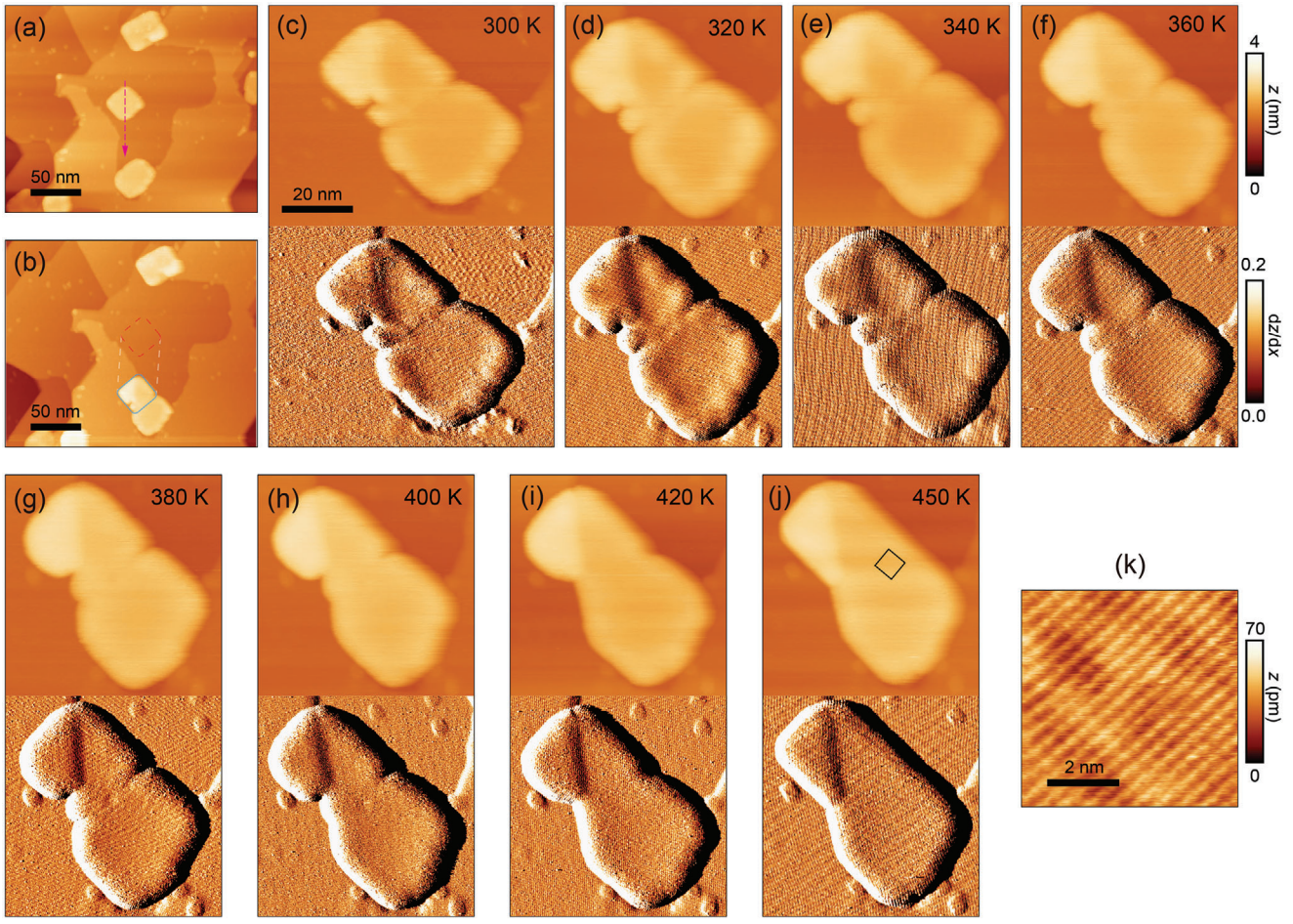

Figure 4. Nanowelding of two SnSe bilayer nanoplates. a) STM topography image showing the starting positions of the nanoplates. $V_s = -0.35$ V, $I_t = 2$ pA. The magenta dashed arrow indicates the path of the tip. The parameters used for pushing the nanoplate are $V_s = -1$ mV, $I_t = 1$ nA, $\nu = 5$ nm s^{-1}. b) STM topography image after the nanoplate manipulation. $V_s = -0.4$ V, $I_t = 2$ pA. c–j) STM topography images and the corresponding derivative images of the two contacted nanoplates acquired during the in situ annealing process. $V_s = -0.4$ V, $I_t = 2$ pA. All the images share the same color scale and scale bar. k) Atom resolved image taken from the area in the black square in panel (j). $V_s = -30$ mV, $I_t = 800$ pA.

In principle, the defect-free nanowelding method introduced here can be applied to any nanostructure having a van der Waals interaction with its supporting substrate, as long as anisotropic lubricity exists via near commensuration along one spatial direction. Lateral heterostructures can be generated in a straightforward way if nanoplates of different materials are prepared on the same substrate. Furthermore, if the nanoplates are on an insulating substrate, the structures created by nanowelding can be used as nanodevices, which could be directly characterized by electrical transport experiments.

3. Conclusion

In summary, we have established a method for defect-free nanowelding between 2D semiconducting nanoplates with the assistance of the anisotropic lubricity at the van der Waals interface between a nanoplate and a single-crystal substrate. Nanowelding between bilayer SnSe nanoplates has been experimentally demonstrated by joining these nanoplates along the zigzag direction of graphene with an STM tip and in situ annealing at 420 K. This method is generally applicable to all 2D material interfaces with anisotropic lubricity and has the potential for the creation of nanoscale quantum devices whose features are too small for traditional lithography, such as lateral tunneling junctions and quantum interference loops. This approach is especially suitable for constructing solid state qubits that require the fabrication of ≈10 nm scale structures, such as the Josephson junctions in superconducting qubits, as well as the nanowires and plunge gates in topological qubits and semiconducting qubits.

4. Experimental Section

Density Functional Theory Calculations: Density functional theory calculations were performed using the SIESTA code.[41] The graphene and SnSe monolayer unit cells were relaxed independently until force components were less than 1 meV $Å^{-2}$. The separation between the graphene and the SnSe layers was optimized for the most commensurate orientation to 3.45 Å, and the third lattice vector length was set to 30 Å to avoid interaction among periodic copies. For the commensurate orientation case, a 5 × 1 supercell was used for SnSe on top of a 9 × 1 rectangular

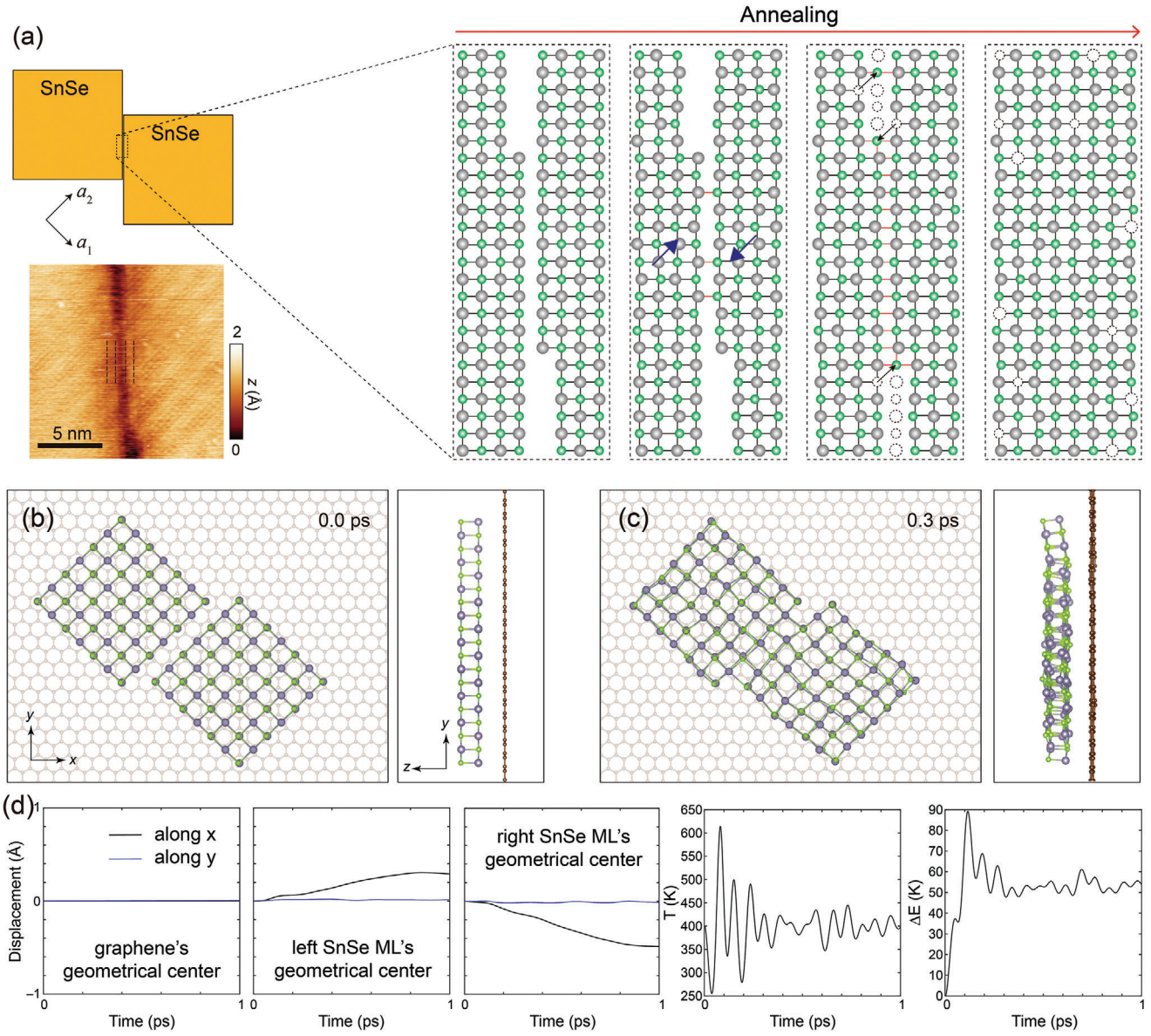

Figure 5. Nanowelding of two monolayer SnSe nanoflakes. a) Schematics of nanowelding achieved by thermal annealing. The four sequential panels in the right reflect the process of interface evolution during annealing. The blue arrows in the second panel indicate the direction of movement of the nanoplates as chemical bonds between the nanoplates form, while the smaller arrows in the third panel indicates examples of possible molecular migration during annealing. For clarity, only the atoms in the topmost layer and the fluctuation along the horizontal direction are shown. The inset atom resolved STM topography image shows the interface between two nanoplates that have been brought into contact. The outermost and third-outmost rows of atoms at the edges are labeled by dashed lines. The manipulation process is described in Figure S6 (Supporting Information). Setpoint: V_s = −0.2 V, I_t = 50 pA. b,c) Structural snapshots along the ab initio molecular dynamics calculation of two monolayer SnSe nanoplates at b) the initial state and c) after 0.3 ps. d) Evolution of several physical parameters during the annealing. The three panels in the left describe the motion of the geometric centers of graphene and the two SnSe nanoplates. The black and blue curves correspond to the motion along *x*- and *y*-directions, respectively. The two panels in the right show instantaneous effective temperature $T(t)$ and total energy with respect to the initial configuration.

supercell for graphene (each rectangular cell of graphene contains four atoms) with a 1 × 15 × 1 Monkhorst–Pack *k*-point mesh and shifted the layers by 1/25 of a graphene rectangular cell lattice vector length until the energy corrugation surface was produced. For the incommensurate orientation case, a 4 × 26 supercell was used for SnSe on top of a 7 × 27 rectangular supercell for graphene with a single *k*-point and shifted the layers in the same way as above. In both cases, a mesh cutoff of 300 Ry, standard double-zeta plus polarization basis sets,[42] and norm-conserving Troullier–Martins pseudopotentials[43] were used with the self-consistent van der Waals exchange correlation functional of Hyldgaard et al.,[44] as implemented by Román-Pérez and Soler.[45] These pseudopotentials were tuned in-house.[46]

Ab Initio Molecular Dynamics: The welding of monolayer SnSe was simulated with ab initio molecular dynamics calculations having a 2 ps time resolution using the NVT ensemble (in which the number of electrons (N), the volume (V), and the temperature (T) are fixed) with the SIESTA code. The model system has the following features: i) it contains two equally sized monolayer SnSe nanoplates with 98 atoms each, originally

placed 2 Å apart, on a graphene substrate containing 1100 atoms; ii) in the experiments, the SnSe nanoplates lie on stiff epitaxial graphene, which itself is grown from SiC. To emulate conditions in which the nanoplates lie on a stiff substrate that only serves as a rail, the carbon positions were effectively fixed in this simulation; iii) temperature only carries meaning at the (macroscopic) thermodynamic limit, where heat can be shared between nanoplates and substrate. Here, by fixing the graphene substrate the SnSe nanoplate is prevented from dissipating heat. Bond energies are strongly dependent on the choice of exchange correlation functional used in ab initio molecular dynamics simulations, so a one-to-one correspondence between experimental and computational temperatures should not be expected. Here, the SnSe monolayer nanoplates and graphene were heated to a target temperature (which was set to be 300 K), and the simulated material was cooled down afterward.

Sample Preparation: SnSe monolayer and bilayer nanoplates were both grown on a graphitized 6H-SiC (0001) substrate by molecular beam epitaxy with a base pressure of 1×10^{-10} mbar. The preparation methods of the graphene substrate and SnSe nanoplates were the same as those described in ref. [37]. The graphene substrate was first degassed at 500 °C for several hours, then annealed at 900 °C in a Si flux for 15 min, and finally annealed at 1400 °C for 10 min. The substrate temperature was measured with an infrared pyrometer. SnSe granules (99.999%, Alfa Aesar) were loaded into an h-BN crucible in a home-built evaporator. The evaporation temperature for SnSe was ≈450 °C. The SnSe monolayer nanoplates were prepared by a two-step method. First, SnSe was deposited onto the graphene substrate at room temperature for 30 s to form the nuclei, then the sample was annealed at 210 °C for 1 h to let the nuclei acquire regular rectangular shapes. Finally, more SnSe was deposited at the substrate of 210 °C, until the desired nanoplate size was reached. Monolayer nanoplates dominate on the substrate after the growth process. To allow for a predominance of bilayer nanoplates, the two-step process was repeated, which allowed for new nuclei to appear on the surface of monolayer nanoplates.

Variable-Temperature STM: The samples were transferred to an Omicron VT-STM-XT system connected to the growth chamber without breaking the ultrahigh vacuum environment. All the STM images were acquired at room temperature unless specified in the figures. The STM system was operated via a Nanonis controller. A Pt/Ir alloy tip was calibrated on the surface of an Au (111) single crystal before scanning. During the dI/dV measurements, a sinusoidal voltage of 30 mV with a 713 Hz frequency was added to the bias voltage. A Lakeshore 335 temperature controller was used to stabilize the sample temperature during the in situ annealing experiments. The relatively large thermal drift at elevated temperatures was eliminated by using a parallelogram correction when processing the images in Figure 4d–j, based on the features of the substrate displayed at room temperature in Figure 4c.

Supporting Information

Supporting Information is available from the Wiley Online Library or from the author.

Acknowledgements

K.C. was supported by National Natural Science Foundation of China (Grants No. 92165104 and 12074038), Beijing Municipal Science & Technology Commission (Grant No. Z221100002722013), and Innovation Program for Quantum Science and Technology (Program No. 2023ZD0300500). S.S.P.P. acknowledges funding from the Deutsche Forschungsgemeinschaft (DFG, German Research Foundation) (Project No. 314790414). J.W.V. and S.B.-L. were funded by the U.S. DOE (J.W.V. by DE-SC0016139, and S.B.-L. by DE-SC0022120). Calculations were performed at Cori at NERSC, a DOE facility funded under Contract DE-AC02-05CH11231, and at the University of Arkansas' Pinnacle supercomputer, funded by the NSF under Award OAC-2346752, the Arkansas Economic Development Commission, and the Office of the Vice Provost for Research and Innovation. The authors thank Shiva P. Poudel for technical assistance.

Open access funding enabled and organized by Projekt DEAL.

Conflict of Interest

The authors declare no conflict of interest.

Data Availability Statement

The data that support the findings of this study are available from the corresponding author upon reasonable request.

Keywords

2D ferroelectrics, anisotropic lubricity, nanowelding, scanning tunneling microscopy, tin selenide

Received: November 15, 2023
Revised: June 3, 2024
Published online:

[1] P. Li, Z. Kang, F. Rao, Y. Lu, Y. Zhang, *Small Methods*. **2021**, *5*, 2100654.
[2] M. Terrones, F. Banhart, N. Grobert, J. C. Charlier, H. Terrones, P. M. Ajayan, *Phys. Rev. Lett.* **2002**, *89*, 075505.
[3] X. Duan, J. Zhang, X. Ling, Z. Liu, *J. Am. Chem. Soc.* **2005**, *127*, 8268.
[4] L. Yang, J. Cui, Y. Wang, C. Hou, H. Xie, X. Mei, W. Wang, K. Wang, *RSC Adv.* **2015**, *5*, 56677.
[5] J. W. Do, N. N. Chang, D. Estrada, F. Lian, H. Cha, X. J. Duan, R. T. Haasch, E. Pop, G. S. Girolami, J. W. Lyding, *ACS Nano*. **2015**, *9*, 4806.
[6] Y. Yao, K. K. Fu, S. Zhu, J. Dai, Y. Wang, G. Pastel, Y. Chen, T. Li, C. Wang, T. Li, L. Hu, *Nano Lett.* **2016**, *16*, 7282.
[7] Z. Gu, H. Ye, D. Smirnova, D. Small, D. H. Gracias, *Small*. **2006**, *2*, 225.
[8] Y. Lu, J. Y. Huang, C. Wang, S. Sun, J. Lou, *Nat. Nanotechnol*. **2010**, *5*, 218.
[9] E. C. Garnett, W. Cai, J. J. Cha, F. Mahmood, S. T. Connor, M. Greyson Christoforo, Y. Cui, M. D. McGehee, M. L. Brongersma, *Nat. Mater.* **2012**, *11*, 241.
[10] T. B. Song, Y. Chen, C. H. Chung, Y. Yang, B. Bob, H. S. Duan, G. Li, K. N. Tu, Y. Huang, Y. Yang, *ACS Nano*. **2014**, *8*, 2804.
[11] D. P. Langley, M. Lagrange, G. Giusti, C. Jiménez, Y. Bréchet, N. D. Nguyen, D. Bellet, *Nanoscale*. **2014**, *6*, 13535.
[12] S. Dai, Q. Li, G. Liu, H. Yang, Y. Yang, D. Zhao, W. Wang, M. Qiu, *Appl. Phys. Lett.* **2016**, *108*, 121103.
[13] X. Liang, T. Zhao, P. Zhu, Y. Hu, R. Sun, C. P. Wong, *ACS Appl. Mater. Interfaces*. **2017**, *9*, 40857.
[14] N. H. Tran, T. H. Duong, H. C. Kim, *Sci. Rep.* **2017**, *7*, 15093.
[15] Z. J. Zhao, M. Gao, S. Hwang, S. Jeon, I. Park, S. H. Park, J. H. Jeong, *ACS Appl. Mater. Interfaces*. **2019**, *11*, 7261.
[16] A. Hu, P. Peng, H. Alarifi, X. Y. Zhang, J. Y. Guo, Y. Zhou, W. W. Duley, *J. Laser Appl.* **2012**, *24*, 042001.
[17] Y. Wu, P. Yang, *Adv. Mater.* **2021**, *13*, 520.
[18] M. A. Van Huis, L. T. Kunneman, K. Overgaag, Q. Xu, G. Pandraud, H. W. Zandbergen, D. Vanmaekelbergh, *Nano Lett.* **2008**, *8*, 3959.
[19] L. Zhang, Y. Tang, Q. Peng, T. Yang, Q. Liu, Y. Wang, Y. Li, C. Du, Y. Sun, L. Cui, F. Yang, T. Shen, Z. Shan, J. Huang, *Nat. Commun.* **2018**, *9*, 96.
[20] M. Hirano, K. Shinjo, *Phys. Rev. B.* **1990**, *41*, 11837.

[21] M. Hirano, K. Shinjo, R. Kaneko, Y. Murata, *Phys. Rev. Lett.* **1991**, *67*, 2642.
[22] Z. Liu, J. Yang, F. Grey, J. Z. Liu, Y. Liu, Y. Wang, Y. Yang, Y. Cheng, Q. Zheng, *Phys. Rev. Lett.* **2012**, *108*, 205503.
[23] P. E. Sheehan, C. M. Lieber, *Science.* **1996**, *272*, 1158.
[24] F. Trillitzsch, R. Guerra, A. Janas, N. Manini, F. Krok, E. Gnecco, *Phys. Rev. B.* **2018**, *98*, 165417.
[25] R. M. Overney, H. Takano, M. Fujihira, W. Paulus, H. Ringsdorf, *Phys. Rev. Lett.* **1994**, *72*, 3546.
[26] M. Liley, D. Gourdon, D. Stamou, U. Meseth, T. M. Fischer, C. Lautz, H. Stahlberg, H. Vogel, N. A. Burnham, C. Duschl, *Science.* **1998**, *280*, 273.
[27] M. Dienwiebel, G. S. Verhoeven, N. Pradeep, J. W. M. Frenken, J. A. Heimberg, H. W. Zandbergen, *Phys. Rev. Lett.* **2004**, *92*, 126101.
[28] J. Y. Park, D. F. Ogletree, M. Salmeron, R. A. Ribeiro, P. C. Canfield, C. J. Jenks, P. A. Thiel, *Science.* **2005**, *309*, 1354.
[29] T. Filleter, J. L. McChesney, A. Bostwick, E. Rotenberg, K. V. Emtsev, T. Seyller, K. Horn, R. Bennewitz, *Phys. Rev. Lett.* **2009**, *102*, 086102.
[30] J. S. Choi, J. S. Kim, I. S. Byun, D. H. Lee, M. J. Lee, B. H. Park, C. Lee, D. Yoon, H. Cheong, K. H. Lee, Y. W. Son, J. Y. Park, M. Salmeron, *Science.* **2011**, *333*, 607.
[31] P. Gallagher, M. Lee, F. Amet, P. Maksymovych, J. Wang, S. Wang, X. Lu, G. Zhang, K. Watanabe, T. Taniguchi, D. Goldhaber-Gordon, *Nat. Commun.* **2016**, *7*, 10745.
[32] F. Long, P. Yasaei, W. Yao, A. Salehi-Khojin, R. Shahbazian-Yassar, *ACS Appl. Mater. Interfaces.* **2017**, *9*, 20922.
[33] Z. Cui, G. Xie, F. He, W. Wang, D. Guo, W. Wang, *Adv. Mater. Interfaces.* **2017**, *4*, 1700998.
[34] Y. Song, D. Mandelli, O. Hod, M. Urbakh, M. Ma, Q. Zheng, *Nat. Mater.* **2018**, *17*, 894.
[35] A. Pacheco-Sanjuan, P. Kumar, S. Barraza-Lopez, *Phys. Rev.* **2024**, *8*, 044001.
[36] J. Wang, A. Khosravi, A. Vanossi, E. Tosatti, *Rev. Mod. Phys.* **2024**, *96*, 011002.
[37] K. Chang, F. Küster, B. J. Miller, J. R. Ji, J. L. Zhang, P. Sessi, S. Barraza-Lopez, S. S. P. Parkin, *Nano Lett.* **2020**, *20*, 6590.
[38] R. C. Sharma, Y. A. Chang, *Bull. Alloy Phase Diagrams.* **1986**, *7*, 68.
[39] M. Mehboudi, B. M. Fregoso, Y. Yang, W. Zhu, A. Van Der Zande, J. Ferrer, L. Bellaiche, P. Kumar, S. Barraza-Lopez, *Phys. Rev. Lett.* **2016**, *117*, 246802.
[40] S. P. Poudel, J. W. Villanova, S. Barraza-Lopez, *Phys. Rev. Mater.* **2019**, *3*, 124004.
[41] M. S. José, A. Emilio, D. G. Julian, G. Alberto, J. Javier, O. Pablo, S.-P. Daniel, *J. Phys.: Condens. Matter.* **2002**, *14*, 2745.
[42] J. Junquera, Ó. Paz, D. Sánchez-Portal, E. Artacho, *Phys. Rev. B.* **2001**, *64*, 235111.
[43] N. Troullier, J. L. Martins, *Phys. Rev. B.* **1991**, *43*, 1993.
[44] P. Hyldgaard, K. Berland, E. Schröder, *Phys. Rev. B.* **2014**, *90*, 075148.
[45] G. Román-Pérez, J. M. Soler, *Phys. Rev. Lett.* **2009**, *103*, 096102.
[46] P. Rivero, V. M. Garcia-Suarez, D. Pereniguez, K. Utt, Y. Yang, L. Bellaiche, K. Park, J. Ferrer, S. Barraza-Lopez, *Comput. Mater. Sci.* **2015**, *98*, 372.